Theor Chem Acc (2012) 131:1108
DOI 10.1007/s00214-012-1108-z

REGULAR ARTICLE

Theoretical studies on the chemical decomposition of 5-aza-2′-deoxycytidine: DFT study and Monte Carlo simulation

Jie Ying Gao · Xin Yang · Chan Kyung Kim · Ying Xue

Received: 2 August 2011 / Accepted: 18 September 2011 / Published online: 10 February 2012

Abstract The decomposition mechanism of 5-Aza-2′-deoxycytidine has been studied by the use of computational techniques. Optimized structures for all of the stationary points in the gas phase were investigated at B3LYP/6-31+G(d,p) level of theory. Single-point energies were determined employing the ab initio MP2 method in conjunction with the 6-311++G(d,p) basis set. Five possible pathways, paths 1–5, were evaluated. In each pathway, the direct (A-paths 1–5) and water-assisted (B-paths 1–5) processes were considered. Meanwhile, the local microhydration model with the direct participation of three water molecules around the reaction centers was adopted to mimic the system for the water-assisted decomposition mechanisms above, where one water molecule is the nucleophilic reactant and the other two are the auxiliary molecules located on each side of the nucleophilic water. The results in the gas phase exhibit that the energy barriers of the water-assisted pathways based on the local microhydration model decrease dramatically by about 15–20 kcal/mol as compared with those of the direct pathways because of the contribution of the auxiliary water molecules. In addition, bulk solvent effects of water were determined by means of the self-consistent reaction field based on the conductor-like polarized continuum model and Monte Carlo simulation with free energy perturbation (MC-FEP) technique, respectively. Our computational results indicate that B-path 3 in the decomposition reaction of 5-azadC is the most favorable, where the calculated rate constant (1.68×10^{-3} min^{-1}) using the MC-FEP method is within the range of the experimentally determined values [$(5.89 \pm 0.54) \times 10^{-3}$ min^{-1} by UV and $(1.46 \pm 0.08) \times 10^{-3}$ min^{-1} by NMR].

Keywords 5-Aza-2′-deoxycytidine · Decomposition mechanism · Microhydration model · Self-consistent reaction field · Monte Carlo simulation

1 Introduction

5-Aza-2′-deoxycytidine (5-azadC) is a cytosine nucleoside analogue, which was originally synthesized as an anticancer agent [1]. 5-azadC has demonstrated its most positive effect in the clinical treatment for myelodysplastic syndrome (MDS) [2–5], for which it received approval by the US Food and Drug Administration in 2004. Meanwhile, the great attention was also paid to clinical investigation of 5-azadC for the treatment for other human cancers such as metastatic lung cancer [6] and hormone-independent prostate cancer [7]. Clinically, aberrant DNA methylation patterns are frequently observed in numerous human cancers [8]. 5-azadC has high toxicity and has long been utilized as a DNA methyltransferase inhibitor through inhibiting aberrant DNA methylation and then re-activating numerous silenced tumor suppressor genes [9].

Electronic supplementary material The online version of this article (doi:10.1007/s00214-012-1108-z) contains supplementary material, which is available to authorized users.

J. Y. Gao · X. Yang · Y. Xue (✉)
College of Chemistry, Key Lab of Green Chemistry and Technology in Ministry of Education, Sichuan University, Chengdu 610064, People's Republic of China
e-mail: yxue@scu.edu.cn

C. K. Kim
Department of Chemistry, Inha University, Incheon 402-751, Korea

Y. Xue
State Key Laboratory of Biotherapy, Sichuan University, Chengdu 610041, People's Republic of China

In aqueous solution, 5-azadC is quite unstable and rapidly decomposes within hours. The facile decomposition of 5-azadC in DNA has recently been the one of the primary hindrance on clinical development of 5-azadC from pharmacology and toxicology testing to clinical trials [10–14]. Early reviews showed that the decomposition products of 5-azadC themselves are likely to be bioactive and toxic-independent of the parent compound [15, 16], thus bringing about another problem whether 5-azadC or its decomposition products may have pharmacokinetic activity, or both. From then on, the decomposition reaction of 5-azadC was the focus of many experimental research groups due to its clinical importance, but there was a disagreement about the identification of decomposition products of 5-azadC [15–17]. In 1981, Lin et al. [15] examined the chemical stability of 5-azadC in acidic, neutral, and alkaline solutions by high-performance liquid chromatographic analysis. They reported that the decomposition of 5-azadC begins with the reversible hydrolytic opening, followed by irreversible deformylation of the triazine ring to give the final product 1-beta-D-2′-deoxyribofurano-syl-3-guanylurea (see Scheme 1). In their experiment, the ring-opening-formylated intermediate formyl-1-beta-D-2′-deoxyribofuranosyl-3-guanylurea and other three unknown compounds were detected in neutral solution (or water). Later, Vesely et al. [16] investigated the effect of the α-D-anomer of 5-azadC in mouse leukemic cells, suggesting that anomerization to α-azadC accounts for at least one of the previously unknown decomposition products in Lin's work. In 2006, Liu et al. [17] developed a new liquid chromatography/tandem mass spectrometry (HPLC/MS/MS) method for studying the pharmacokinetics of 5-azadC in plasma. They pointed out that those previously unidentified compounds are isomers of the ring-opening-formylated intermediate formyl-1-beta-D-2′-deoxyribofuranosyl-3-guanylurea or products 1-beta-D-2′-deoxyribofuranosyl-3-guanylurea. They proposed two plausible decomposition mechanisms for 5-azadC: (1) 1,2-addition with the nucleophilic attack of the water molecule at $C_{(1)}$ atom and the simultaneous proton transfer to $N_{(2)}$ atom; (2) 1,4-addition with a nucleophilic water molecule attacking at $C_{(1)}$ atom and proton shift to $N_{(4)}$ atom. The preference of the nucleophilic attack of hydroxyl ion at first to $C_{(1)}$ mainly attributes to the lower electron density in position 1 in 5-azadC, which has been substantiated by Pithova's investigation [18]. Recently, Rogstad et al. [19] used multiple analytical techniques involving NMR, HPLC, and mass spectrometry to estimate the kinetic rates and characterize the decomposition products under conditions of physiological temperature and pH. The rate constants for the two decomposition processes of 5-azadC (see Scheme 1) were obtained in their experiment, which are in good agreement with those values inferred from the first-order exponential decay equation.

However, to the best of our knowledge, the detailed decomposition mechanism of 5-azadC has remained elusive and no related theoretical work has been reported. In the present study, we first examine the first step (process 1 in Scheme 1) of the complex reaction process that is the decomposition of 5-azadC to the ring-open-formylated compound, to determine the ring-open-formylated intermediate of decomposition and further identify the corresponding decomposition products of 5-azadC. To fully illuminate the title reaction, we would like to perform a detailed computational study for the five possible mechanisms (paths 1–5), as shown in Scheme 2. For the gas-phase reactions, the structures for all of the stationary points were optimized at the density functional theory B3LYP/6-31+G(d,p) level followed by the single-point MP2/6-311++G(d,p) calculations to obtain more credible energy information. The direct and the water-assisted decomposition were considered. Taking the major effect of the inner solvent layer on the energy barrier into account, an interesting local microhydration model was constructed to describe the water-assisted mechanism with three water molecules around the reaction centers. Among them, in each step, one is the nucleophilic reactant, another serves as the bridge to help the transfer of the hydrogen atom, and the third one makes the cooperative effect to stabilize the structure through forming the hydrogen bond in the opposite side near to the nonreactive nitrogen atom (see Scheme 3). This model has been utilized in our previous

Scheme 1 Decomposition of 5-azadC to the guanylurea compound

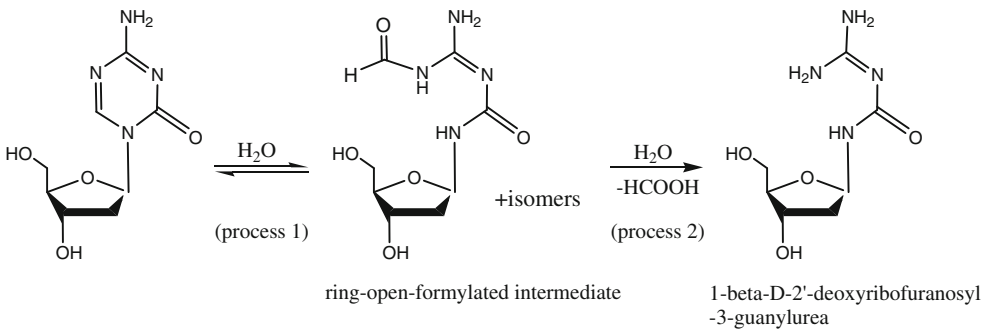

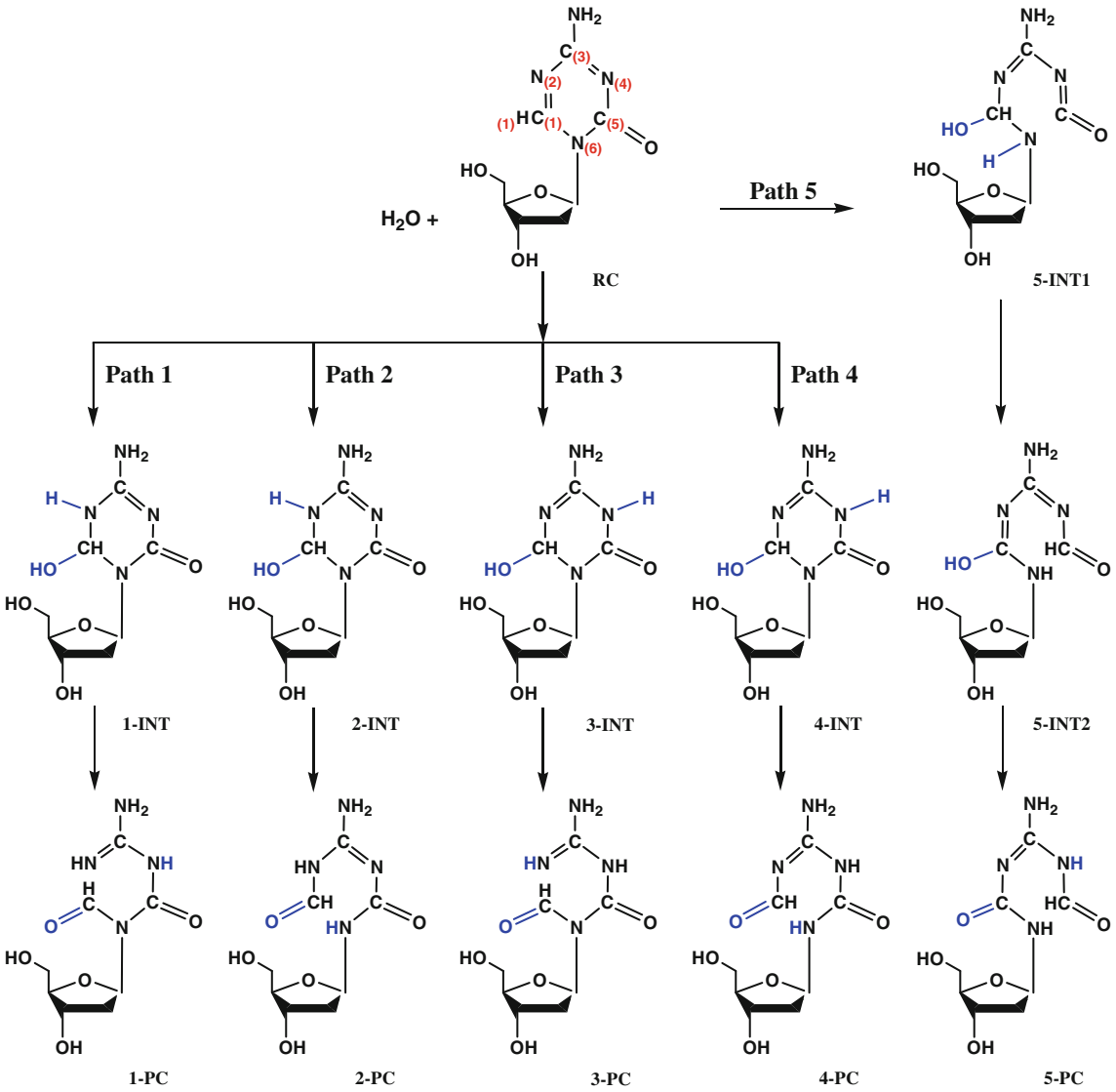

Scheme 2 Possible five decomposition pathways of 5-azadC

Scheme 3 Schematic local microhydration model for the water-assisted decomposition of 5-azadC (using B-path 2 as an example)

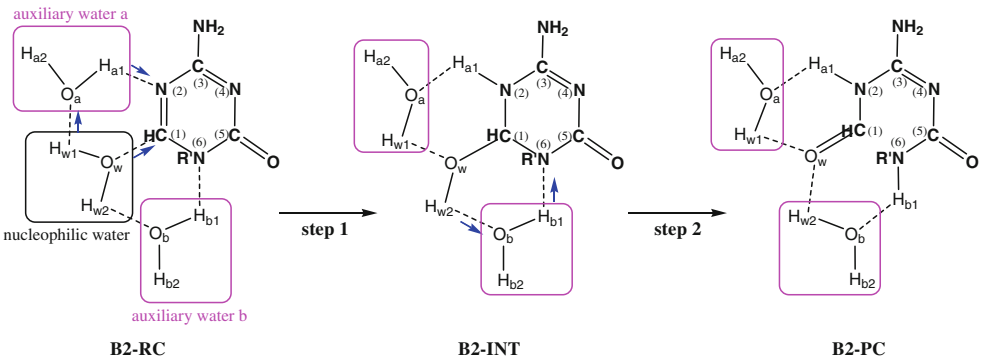

study for the water-assisted hydrolysis of *N*,*N*-dimethyl-*N*′-(2′,3′-dideoxy-3′-thiacytidine) formamidine [20]. Additionally, it is well known that bulk solvent effects play an important role in determining transition states (TS), reaction rates, equilibrium constants, and the other quantities of chemical and biochemical processes. In our previous work, we adopted the quantum chemical molecular orbital method and Monte Carlo (MC) simulation with free

energy perturbation (FEP) technique to study solvent effects on a series of systems involving the aza-Wittig reaction of iminophosphoranes [21], the isomerization of imidazolines [22, 23], the hydrolysis of *N*-(2-oxo-1,2-dihydro-pyrimidinyl) formamide [24], the aminolysis of $XC(O)OCH_3$ [25], and the hydrolytic deamination of 5-methylcytosine glycol [26]. In this study, the effect of water as solvent was studied using the Monte Carlo free energy perturbation method (MC-FEP) and the self-consistent reaction field (SCRF) method based on the conductor-like polarized continuum model (CPCM). Such calculations provide a detailed mechanism of this reaction and identify the ring-open-formylated intermediate of decomposition, which facilitate ongoing determination of corresponding decomposition products of 5-azadC.

2 Computational details

2.1 Gas-phase calculations

To assess the sensitivity of structures to the method and basis set choice, a variety of computational levels involving HF, B3LYP, BHandHLYP, and MP2, and two basis sets [6-31+G(d,p) versus 6-311++G(d,p)] were used to optimize the geometry of 5-zazdC based on the X-ray crystallographic structure. Comparison of the results obtained by the methods above indicated that the B3LYP/6-31+G(d,p) level is acceptable and a relatively reliable option in this work (see the detailed discussion in the Sect. 3.1). Therefore, the B3LYP/6-31+G(d,p) method was chosen for the ensuing calculations on the title reactions.

The geometric structures of all the reactant complexes (RC), transition states, intermediates (INT), and product complexes (PC) in the direct and water-assisted pathways in the gas phase were optimized at the B3LYP/6-31+G(d,p) level. The harmonic vibrational frequencies were also calculated at the same level to characterize the nature of the stationary points as true minimum with no imaginary or transition state with only one imaginary frequency and to provide thermodynamic quantities such as the zero-point vibrational energy, thermal correction, enthalpies, Gibbs free energies, and entropies. Single-point MP2 calculations, MP2/6-311++G(d,p)//B3LYP/6-31+G(d,p), were also carried out to assess the accuracy of the B3LYP energies.

All transition states were checked by the intrinsic reaction coordinate (IRC) calculations [27]. In the IRC calculations for the decomposition reaction systems, "IRC = tight" option was used to generate the minimum energy path (MEP) in the gas phase. The MEPs at the B3LYP/6-31+G(d,p) level were constructed with a step size of 0.05 $amu^{1/2}$ bohr, and the partial charges were calculated for all points along the MEP using the CHELPG method [28]. All calculations mentioned above were performed with the Gaussian 03 program [29].

2.2 Solvation calculations

2.2.1 CPCM

The solvent effects of water on five direct pathways (A-paths 1–5) and five water-assisted pathways (B-paths 1–5) were tested by the SCRF method based on the CPCM [30]. Single-point energy calculations were performed in water at the MP2/6-311++G(d,p) level of theory on the basis of the gas-phase optimized geometries. The dielectric constant used in the calculations was $\varepsilon = 78.39$ for water. Both zero-point vibrational energies and thermal corrections at 298.15 K and 1 atm obtained at the B3LYP/6-31 + G(d,p) level were used to correct electron energies of single-point calculations.

2.2.2 Monte Carlo simulation

The free energy changes of solvation along the MEP were also determined using Monte Carlo simulation with free energy perturbation [31] method (MC-FEP). The reaction system obtained by DFT studies was immersed in a pre-equilibrated box containing explicit solvent water molecules, and the intermolecular interaction is described by a molecular mechanical potential consisting of Coulomb and Lennard-Jones terms between atom i in molecule a and atom j in molecule b, which are separated by a distance r_{ij} as shown in Eq. 1

$$\Delta E_{ab} = \sum\sum \left\{ q_i q_j e^2 / r_{ij} + 4\varepsilon_{ij} \left[(\sigma_{ij}/r_{ij})^{12} - (\sigma_{ij}/r_{ij})^{6} \right] \right\} \quad (1)$$

where q_i is the partial charge of atom i obtained from the gas-phase calculation above. The crossing terms were obtained using the geometric combining rules:

$$\varepsilon_{ij} = \sqrt{\varepsilon_i \varepsilon_j}, \quad \sigma_{ij} = \sqrt{\sigma_i \sigma_j} \quad (2)$$

The ε and σ constants for the solute were taken from the OPLS all-atom [32] parameters of BOSS program database. The four-site TIP4P model [33–35] was used for the solvent water. The system was perturbed between adjacent structural points i and j, and the free energy differences ΔG_{ij} were calculated via Zwanzig perturbation expression [36] as follows:

$$\Delta G_{ij} = G_j - G_i = -k_B T \ln(\exp(-(E_j - E_i)/k_B T))_i \quad (3)$$

In Eq. 3, E_i is the total energy of the point i, k_B is the Boltzman constant, and T is the absolute temperature.

In this study, 390 water molecules in an approximate $20 \times 20 \times 30$ $Å^3$ box were used for the water-assisted

decomposition reactions. Simulations were carried out in the isothermic–isobaric ensemble (NPT; 1 atm, 298.15 K) by the use of Metropolis sampling and periodic boundary conditions. The solvent–solvent (RCUT) and solute–solvent (SCUT) nonbonded cutoff were both set to 12.0 Å. Preferential sampling was employed with the WKC parameter set to 300. Perturbations were performed using double-wide sampling scheme [31]. The geometries of solute were mutated along the simulation, which were obtained in IRC calculations at the B3LYP/6-31+G(d,p) level in the gas phase. No sampling of the internal degrees of freedom was performed. Each simulation involved 10^6 configurations of equilibration and 2×10^6 configurations of averaging. Parameters determining volume changes and solute rotations and translations were adjusted to have an acceptance level ca. 40%. The total potential energy profile along the reaction path in solution was obtained by adding the gas-phase relative energies to the computed free energy changes of solvation. All of the simulations were executed using the BOSS 4.2 program [37].

3 Results and discussions

3.1 Test calculations

To test the reliability of the computational approaches and basis sets for the calculation of the title reaction, the geometry of 5-zazdC based on the X-ray crystallographic structure was optimized at the different computational methods (HF, B3LYP, BHandHLYP, and MP2) and basis sets [6-31+G(d,p) and 6-311++G(d,p)]. The differences in the bond lengths, bond angles, and torsion angles between the crystal structure and theoretical geometry of 5-azadC are listed in Tables s1–s3 in the Supporting Information. The *D* value in the Supporting Information is defined to evaluate the results at a variety of computational levels above. From Tables s1–s3, it can be seen that, for the four tested approaches (HF, B3LYP, BHandHLYP, and MP2), the structural parameters performed from 6-31+G(d,p) basis set are close to those derived from 6-311++G(d,p) basis set. In Table s1, the computed bond lengths from the B3LYP and MP2 methods are nearly equivalent and both closer to the crystal values in comparison with those derived from the BHandHLYP and HF methods. Among the eight computational levels, the *D* values from the B3LYP/6-31+G(d,p) and MP2/6-31+G(d,p) levels of theory are lower than those obtained from other six levels. Furthermore, comparison of B3LYP and MP2 method, it is found that the MP2 method has the slightly higher *D* values for describing the bond angles of 5-azadC, as listed in Table s2. In addition, two torsional angles (H13-C12-N11-C9 and O14-C12-N11-C2) are taken into account, which are mainly influenced by the intermolecular interactions in the crystal. From Table s3, one can see that out of four examined approaches, the *D* values performed from the B3LYP method are still lower than those derived from other three methods for depicting the torsion angles of 5-azadC. Therefore, it can be concluded that the B3LYP/6-31+G(d,p) approach is suitable for this work with a good compromise between accuracy and computational cost.

3.2 Optimized structures and energetics in the gas phase

3.2.1 Direct decomposition reaction of 5-azadC

As illustrated in Scheme 2, in our work, five possible decomposition pathways of 5-azadC were clarified, denoted as A-paths 1–5. A-path 1 begins with the addition of H_2O to the $C_{(1)}$=$N_{(2)}$ double bond to form a tetrahedral structure A1-INT. And then, the hydroxyl H atom transfers to the $N_{(4)}$ atom to give the final product A1-PC. A-path 2 begins with the addition of H_2O to the $C_{(1)}$=$N_{(2)}$ double bond to form a tetrahedral structure A2-INT, followed by the transfer of hydroxyl H atom to the $N_{(6)}$ atom leading to the product A2-PC. A-path 3 simultaneously contains the nucleophilic attack of the water molecule to the $C_{(1)}$ atom and the proton transfer toward the $N_{(4)}$ atom. Sequentially, the H atom of hydroxyl transfers to the $N_{(2)}$ atom to generate the product A3-PC. A-path 4 simultaneously contains the nucleophilic attack of H_2O to the $C_{(1)}$ atom and the movement of one H atom of water toward the $N_{(4)}$ atom. In the subsequent step, the H atom of hydroxyl transfers to the $N_{(6)}$ atom to generate the product A4-PC. A-path 5 proceeds via three processes. In the first step, the H_2O attacks to the $C_{(1)}$–$N_{(6)}$ single bond leading to the cleavage of the $C_{(5)}$–$N_{(6)}$ bond. Then, one H atom attached to $C_{(1)}$ shifts toward the $C_{(5)}$ atom to produce the intermediate A5-INT2. At last, the proton migration of hydroxyl H atom to the $N_{(4)}$ atom generates the final product A5-PC. These five pathways are the stepwise processes.

The potential energy surface and optimized geometries along with some selected structural parameters for the stationary points are depicted in Figures s1–s5. Cartesian coordinates optimized for the direct decomposition of 5-azadC in the gas phase are given in the Supporting Information. Additional energy data, including the zero-point vibrational energy and thermal corrections (ΔE), and Gibbs free energies (ΔG) are listed in Table 1. From Table 1, it can be seen that, in A-path 1, the relative energy of the second transition state A1-TS2 is 49.2 kcal/mol at the B3LYP method and 48.2 kcal/mol at the MP2 method. It is higher than that in the corresponding first transition state, indicating that the rate-limiting process of A-path 1 is the second-step reaction. In A-path 2, the second step

Table 1 Relative energies, free energies, and solvation energies in direct decomposition of 5-azadC

Direct	B3LYP		MP2		CPCM
	ΔE (gas)	ΔG (gas)	ΔE (gas)	ΔG (gas)	ΔG (sol)
A-path 1					
A1-RC	0.00	0.00	0.0	0.0	0.0
A1-TS1	43.1	46.1	47.0	50.1	48.8
A1-INT	12.8	15.2	11.0	13.5	5.3
A1-TS2	49.2	51.4	48.1	50.4	40.1
A1-PC	12.8	13.5	14.2	14.9	14.2
A-path 2					
A2-RC	0.0	0.0	0.0	0.0	0.0
A2-TS1	43.1	46.1	47.0	50.1	48.8
A2-INT	12.8	15.2	11.0	13.5	5.3
A2-TS2	52.0	55.2	50.2	53.3	48.6
A2-PC	4.2	4.4	9.7	9.9	4.8
A-path 3					
A3-RC	0.0	0.0	0.0	0.0	0.0
A3-TS1	53.1	55.7	50.9	53.5	52.2
A3-INT	8.3	10.7	4.6	7.0	4.3
A3-TS2	44.6	47.6	44.4	47.4	43.6
A3-PC	16.5	17.5	14.1	15.1	14.2
A-path 4					
A4-RC	0.0	0.0	0.0	0.0	0.0
A4-TS1	58.9	59.8	56.9	57.7	51.5
A4-INT	15.0	16.1	10.9	12.0	4.7
A4-TS2	44.0	44.0	47.2	47.3	39.3
A4-PC	12.2	11.7	17.2	16.6	12.1
A-path 5					
A5-RC	0.0	0.0	0.0	0.0	0.0
A5-TS1	57.5	60.1	57.4	60.0	59.0
A5-INT1	30.7	31.5	24.3	25.2	29.6
A5-TS2	43.3	45.2	42.4	44.3	44.9
A5-INT2	19.3	20.4	21.7	22.8	22.4
A5-TS3	20.0	21.8	24.6	26.4	24.8
A5-PC	−1.4	−0.2	2.7	3.9	5.6

In kilocalories per mole

referring to the transfer of H_{w2} of the water molecule is the rate-limiting process, because its relative energy (being 52.0 kcal/mol at B3LYP method and 50.2 kcal/mol at MP2 method) is higher than that in the corresponding first transition state. In A-path 3, the relative energy of the first transition state A3-TS1 is 53.1 kcal/mol at the B3LYP method, while it decreases to 50.9 kcal/mol at the MP2 method. The relative energy of A3-TS1 is higher than that in the corresponding second transition state, implying that the rate-limiting process in this pathway is the first-step reaction. In A-path 4, the first step referring to the nucleophilic attack of H_2O is the rate-limiting process, because its relative energy (58.9 kcal/mol at B3LYP method and 56.9 kcal/mol at MP2 method) is higher than that in the corresponding second transition state. In A-path 5, the first step (the nucleophilic attack of water) is the rate-limiting step with a barrier height of 57.5 kcal/mol at B3LYP method.

From Table 1, the energy barrier in the rate-controlling step of A-path 1 (49.2 kcal/mol) is lower than those of other four pathways (being 52.0, 53.1, 58.9, and 57.5 kcal/mol for A-path 2, A-path 3, A-path 4, and A-path 5, respectively), suggesting that the direct decomposition reaction of 5-azadC in the gas phase may be favorable for A-path 1 than A-paths 2–5. Nevertheless, A-path 1 is still thought to be rather difficult to occur due to the high energy barrier being close to 50 kcal/mol. Such high energy barrier mainly arises from the four-centered transition states. In such cyclic transition states, the orbitals required for the bond dissociation and formation are deformed so much that

a large amount of deformation energy is substantially needed. Therefore, our ensuing work focuses on the examination of the water-assisted decomposition mechanisms of 5-azadC, which are promoted based on a local microhydration model with the introduction of two auxiliary water molecules in the reaction.

3.2.2 Water-assisted decomposition reaction of 5-azadC

In this section, the main structural and energetic features of the water-assisted decomposition mechanism of 5-azadC for the five pathways (B-path 1, B-path 2, B-path 3, B-path 4, and B-path 5) are clarified. Considering the major effect of the inner solvent layer on the energy barrier, a local microhydration model concerning three water molecules around the reaction centers is constructed to describe the system for the five decomposition reaction mechanisms above. As for the two additional water molecules located on each side of the nucleophilic water, one serves as a bridge to help the proton transfer and the other simultaneously makes the cooperative effect to stabilize the structure through forming the hydrogen bond in another side. It is worthwhile to note that, in the next reaction process, the location of the cooperative water just can facilitate to act as a bridge to the subsequent proton transfer while the simultaneous cooperative effect can be afforded by the bridgeable water in last step (see Scheme 3). Under such ingenious model, the consecutive potential energy profiles concerning the two reaction steps (the first is the nucleophilic attack of water and the second is the proton transfer) were obtained. The potential energy surface and optimized geometries along with some selected structural parameters for the stationary points are depicted in Figs. 1, 2, 3, 4, and 5. Cartesian coordinates optimized for the water-assisted decomposition of 5-azadC in the gas phase are given in the Supporting Information. Additional energy data, including the zero-point vibrational energy and thermal corrections (ΔE), and Gibbs free energies (ΔG) are listed in Table 2.

3.2.2.1 B-Path 1 As described in Fig. 1, the reaction proceeds via two processes. In the first step, the reactant complex B1-RC is generated due mainly to the H-bond network, where three water molecules are connected with two hydrogen bonds. Meanwhile, the H_{a1} of one auxiliary water and H_{b1} of the other auxiliary water interact, respectively, with the $N_{(2)}$ atom and the $N_{(4)}$ atom on the pyrimidine ring to form another two hydrogen bonds. Attributed to the presence of an auxiliary water molecule, B1-TS1 is a six-membered ring transition state, which is directly associated with the $C_{(1)}$–O_w bond forming, the H_{w1} atom migration to O_a atom, and the transfer of H_{a1} atom to $N_{(2)}$ atom. IRC results (Fig. 6) indicate that three processes occur simultaneously in this reaction step: the O_w atom attacks at the $C_{(1)}$ atom, the H_{w1} atom transfers from O_w toward O_a atom, and the H_{a1} atom shifts from O_a to $N_{(2)}$ atom. At the same time, the other auxiliary water located in another side of OH group exerts great contribution to keeping the nucleophilic water molecule in an efficient position, forming two hydrogen bonds with the distance of 2.098 and 1.470 Å, respectively. After surmounted the transition state B1-TS1, the intermediate B1-INT is obtained. B1-INT is a tetrahedral geometry similar to that in the direct decomposition mechanism with one water molecule. For the geometry

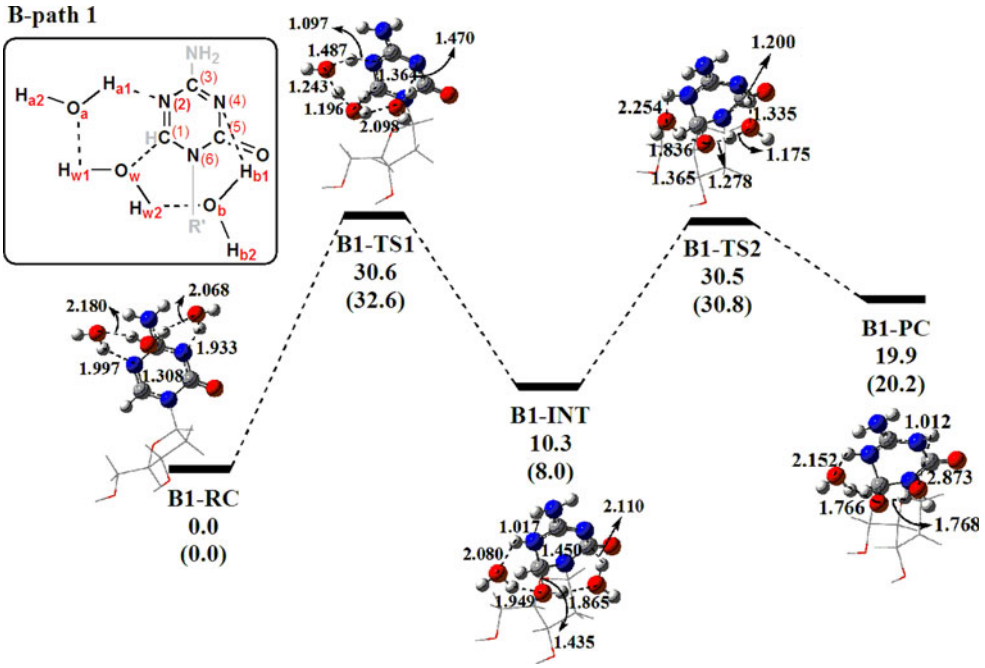

Fig. 1 Potential energy surface (in kcal/mol) and optimized structures (in Å) in B-path 1 for water-assisted decomposition mechanism of 5-azadC in the gas phase (*top values*, ΔG at the B3LYP/6-31+G(d,p) level; value in parentheses, ΔG at the MP2/6-311++G(d,p)//B3LYP/6-31+G(d,p) level)

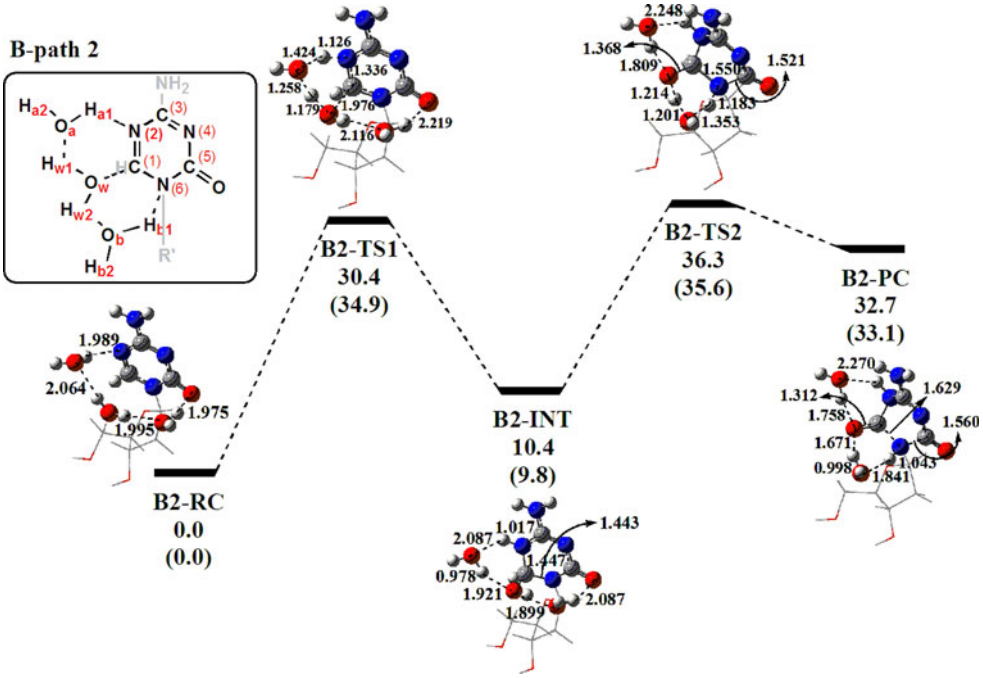

Fig. 2 Potential energy surface (in kcal/mol) and optimized structures (in Å) in B-path 2 for water-assisted decomposition mechanism of 5-azadC in the gas phase

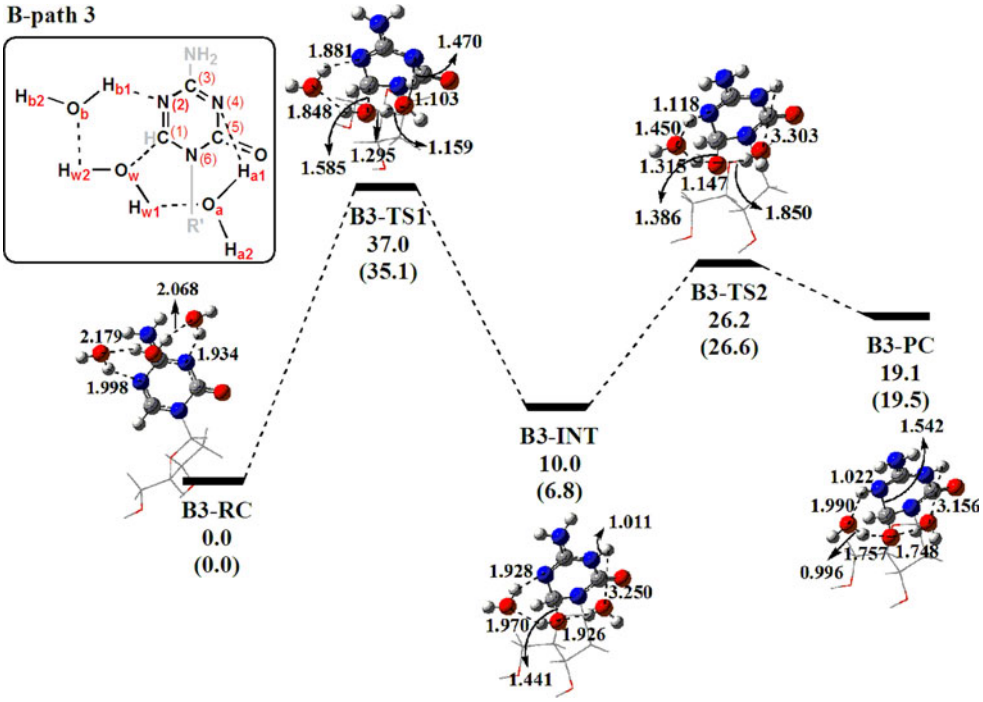

Fig. 3 Potential energy surface (in kcal/mol) and optimized structures (in Å) in B-path 3 for water-assisted decomposition mechanism of 5-azadC in the gas phase

of B1-INT, the distance of $C_{(1)}$–$N_{(2)}$ is 1.450 Å, longer than that in B1-RC by 0.142 Å because the hybridization of $C_{(1)}$ atom changes from sp^2 in B1-RC to sp^3 in B1-INT. Although the distance of H_{b1}–$N_{(4)}$ is 2.110 Å in B1-INT, it also indicates that the H_{b1} atom can be transferred from O_b to $N_{(4)}$ atom due to the short distance. In this process, the energy barriers are 28.8 and 30.8 kcal/mol at the B3LYP and MP2 levels, respectively. The entropic contributions tend to ratherish increase the energy barriers, the Gibbs free energy barrier ascending to 30.6 kcal/mol at the B3LYP level and 32.6 kcal/mol at the MP2 level. In the next step, the transition state B1-TS2, still a six-membered transition state, is located in our calculations. It is worthwhile noting that the auxiliary water, used to stabilize the structure in the first process, severs as a bridge to help the proton transfer of H_{w2} in this step, and at the same time, the structure is stabilized by the bridgehead water that is used in the first process. The imaginary frequency of B1-TS2 is 1,306.64 icm^{-1}, which is associated

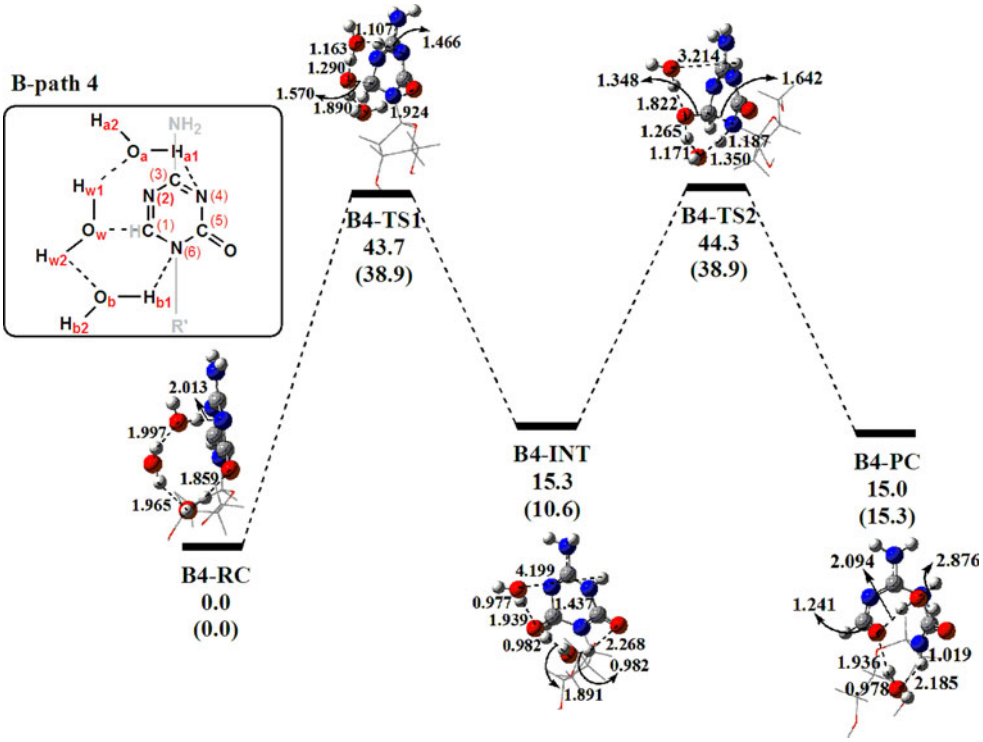

Fig. 4 Potential energy surface (in kcal/mol) and optimized structures (in Å) in B-path 4 for water-assisted decomposition mechanism of 5-azadC in the gas phase

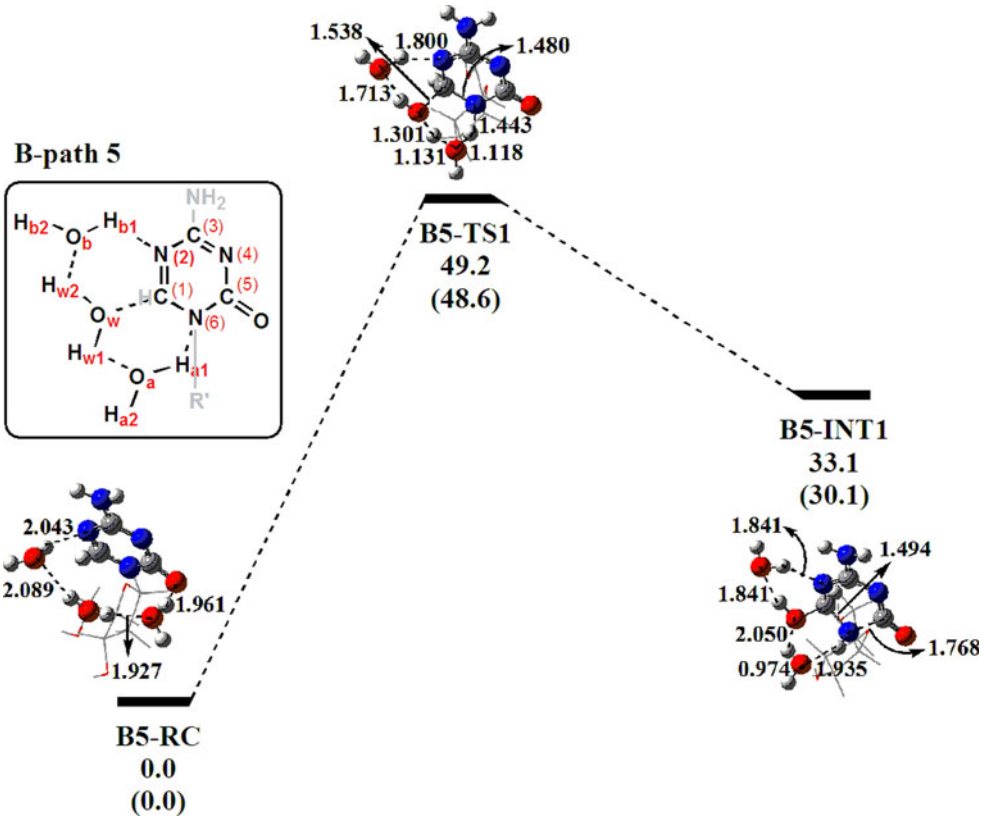

Fig. 5 Potential energy surface (in kcal/mol) and optimized structures (in Å) in the rate-limiting step of B-path 5 for water-assisted decomposition mechanism of 5-azadC in the gas phase

with the coupling of the transfer of H_{b1} atom from O_b to $N_{(4)}$ atom and the transfer of H_{w2} atom from O_w to O_b atom. The geometry of B1-TS2 reflects that the H_{b1} atom can effectively head toward the lone pair of $N_{(4)}$ with a little angle constraint (the bond angle O_b–H_{b1}–$N_{(4)}$ is 151.1°). Finally, the product B1-PC is offered after surmounted the transition state

Table 2 Relative energies, free energies, and solvation energies in water-assisted decomposition of 5-azadC

Water-assisted	B3LYP		MP2		CPCM	Monte Carlo	
	ΔE (gas)	ΔG (gas)	ΔE (gas)	ΔG (gas)	ΔG (sol)	Δ (ΔG(sol))	ΔG (tot)
B-path 1							
B1-RC	0.00	0.0	0.0	0.0	0.0	0.0	0.0
B1-TS1	28.8	30.6	30.8	32.6	30.9	−3.5	27.1
B1-INT	9.0	10.3	6.8	8.0	4.0	0.4	10.7
B1-TS2	27.5	30.5	27.8	30.8	26.4	2.6	33.1
B1-PC	18.7	19.9	19.0	20.2	13.4	−0.4	19.5
B-path 2							
B2-RC	0.0	0.0	0.0	0.0	0.0	0.0	0.0
B2-TS1	27.9	30.4	32.4	34.9	34.6	−0.6	29.8
B2-INT	8.7	10.4	8.1	9.8	8.4	0.8	11.3
B2-TS2	32.7	36.0	32.2	35.6	37.7	5.7	41.7
B2-PC	30.8	32.7	31.3	33.1	36.3	4.6	37.3
B-path 3							
B3-RC	0.0	0.0	0.0	0.0	0.0	0.0	0.0
B3-TS1	34.2	37.0	32.3	35.1	28.2	−17.4	19.6
B3-INT	9.6	10.0	6.4	6.8	1.9	−12.6	−2.6
B3-TS2	24.2	26.2	24.5	26.6	19.5	−11.1	15.2
B3-PC	18.5	19.1	19.0	19.5	12.0	−15.8	3.3
B-path 4							
B4-RC	0.0	0.0	0.0	0.0	0.0	0.0	0.0
B4-TS1	38.7	43.7	34.0	38.9	36.7	−2.2	41.5
B4-INT	12.9	15.3	8.2	10.6	8.1	0.8	16.1
B4-TS2	40.2	44.3	34.7	38.9	35.3	0.8	45.1
B4-PC	12.9	15.0	13.2	15.3	15.3	−2.1	12.0
B-path 5							
B5-RC	0.0	0.0	0.0	0.0	0.0	0.0	0.0
B5-TS1	46.0	49.2	45.3	48.6	41.9	−4.4	44.8
B5-INT1	31.1	33.1	28.1	30.1	31.9	8.6	41.7

In kilocalories per mole

B1-TS2. In B1-PC, the $N_{(4)}$–H_{b1} distance is 1.012 Å, which indicates that this bond has already been shaped. The $C_{(1)}$–O_w bond length is 1.317 Å. It is shortened by 0.048 Å compared to that of the B1-TS2, implying that the bond $C_{(1)}$–O_w changes from the single bond to the double bond. From Table 2, one can see that the nucleophilic attack of the water molecule (the first step) is the rate-limiting process in the gas phase with a barrier height of 28.8 kcal/mol.

3.2.2.2 B-Path 2 In the reactant complex B2-RC, arising from the hydrogen-bonded network involving three water molecules, the nucleophilic water holds a more effective position for the subsequent attacking, with $C_{(1)}$–O_w distance of 3.110 Å. The O_w atom of the nucleophilic water attacks at the $C_{(1)}$ atom, leading to a new six-membered cycle transition state B2-TS1. The calculated imaginary frequency of 1,019.41 icm^{-1} together with its vibrational mode signifies a strong interaction between the nucleophilic water molecule and the $C_{(1)}$ atom. IRC results in Fig. 6 manifest that the three processes occur in concert: the O_w attacks at the $C_{(1)}$ atom, the H_{w1} moves to O_a atom, and the H_{a1} migrates toward the $N_{(2)}$ atom. After passing through B2-TS1, a tetrahedral intermediate B2-INT is offered. The dihedral angle $N_{(6)}$–$N_{(2)}$–$C_{(3)}$–$C_{(1)}$ of −20.1° reflects that the $C_{(1)}$ atom has been deviated from the plane of pyrimidine ring. In this process, the energy barrier is 27.9 kcal/mol at the B3LYP level, while it increases to 32.4 kcal/mol at the MP2 level. When proceeding from B2-INT to B2-TS2, similar to the mechanism of B-path 1, a six-membered ring transition state is also shaped. The imaginary frequency is 1,195.09 icm^{-1}, which is associated with the coupling of the movement of H_{b1} atom from O_b to $N_{(6)}$ atom and the migration of H_{w2} atom from O_w to O_b atom, which then intrigues the rupture of $C_{(1)}$–$N_{(6)}$ bond. Due to the proton transfer, the $C_{(1)}$–$N_{(6)}$ bond distance is elongated by 0.107 Å and the $C_{(1)}$–O_w bond length is shortened by 0.071 Å compared to that of the B2-INT. And then, IRC calculation toward product induces the

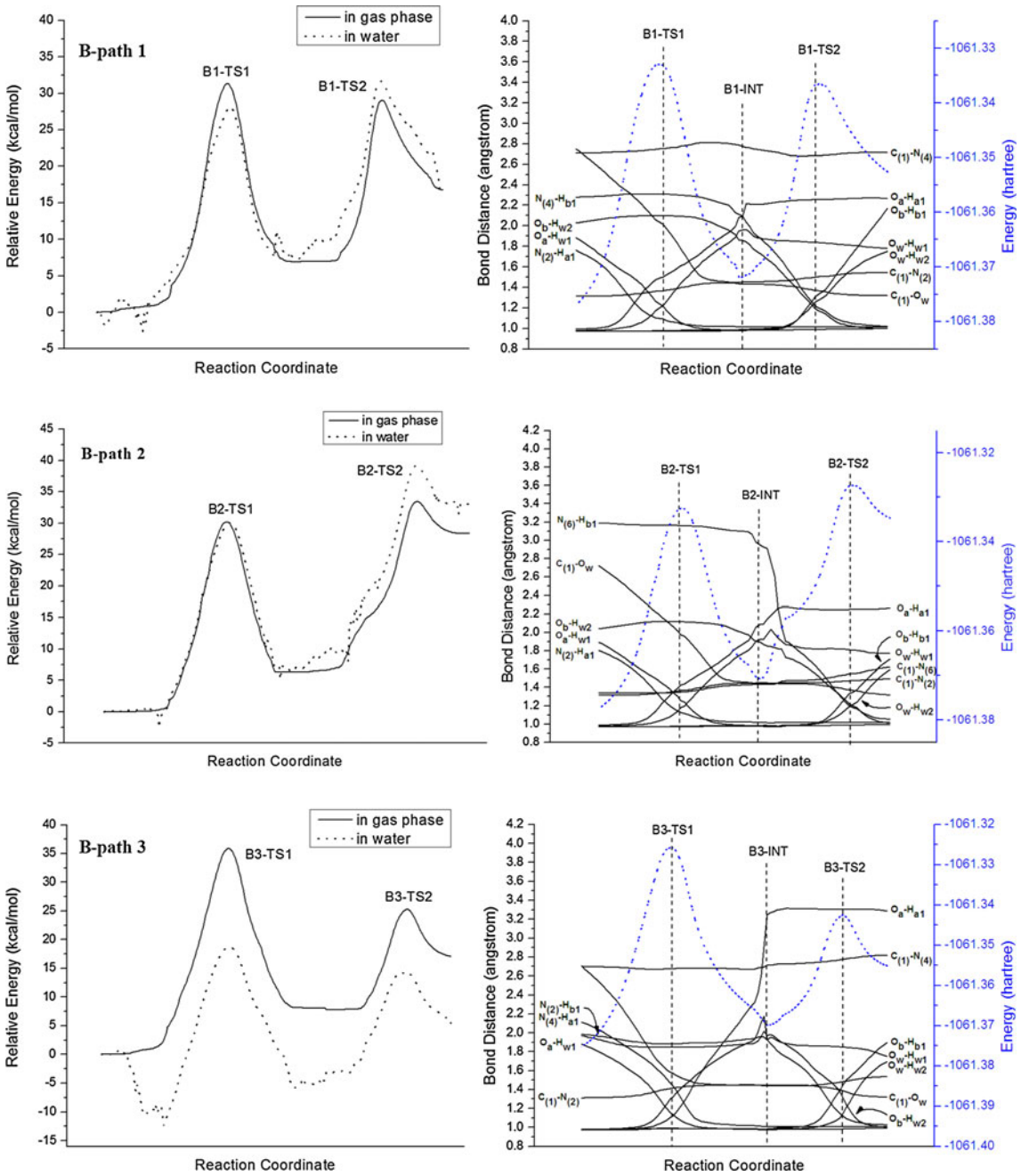

Fig. 6 Changes of the free energies of salvation along the reaction coordinate calculated from Monte Carlo simulations and selected bond lengths (angstrom) along the potential energy profile for the water-assisted decomposition reaction of 5-azadC

appearance of a ring-opening B2-PC (the length of $C_{(1)}$–$N_{(6)}$ bond is 1.629 Å). For B2-PC, the bond $C_{(1)}$–O_w has changed from the single bond to the double bond. Compared to B2-INT, the $C_{(1)}$–O_w bond length is shortened to 1.312 Å by a reduction of 0.127 Å, implying that the acyl group has fully been formed in B2-PC. In this pathway, the second step corresponding to the proton transfer is the rate-determining step with a barrier height of 32.7 kcal/mol in the gas phase.

3.2.2.3 B-Path 3 For the B3-RC, the two auxiliary waters, respectively, occupy one side of nucleophilic water for a compact H-bond network around the $N_{(2)}$ atom and the $N_{(4)}$ atom. We located the transition state B3-TS1 in our calculation. It is also a six-centered ring structure with regard to with the nucleophilic attack of the O_w atom to the $C_{(1)}$ atom and a double proton (H_{w1} and H_{a1}) transfer through a proton bridge, receiving a proton and donating one in turn. In the forward reaction direction, a tetrahedral

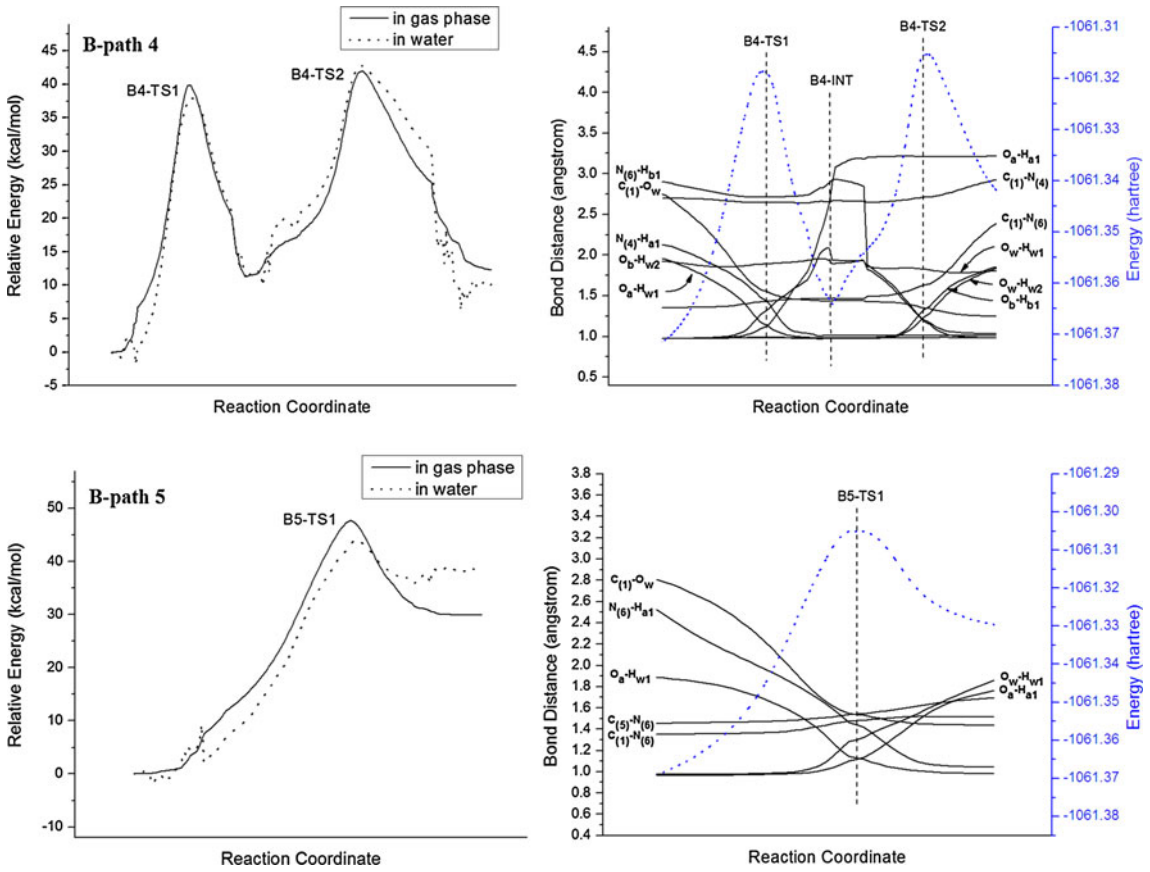

Fig. 6 continued

intermediate B3-INT is obtained. The $C_{(1)}$ atom deviates relatively to $N_{(6)}$–$N_{(2)}$–$C_{(3)}$ plane by ca. 16° rendering the appearance of a tetrahedral structure in B3-INT, together with the disappearance of the $C_{(1)} = N_{(2)}$ double bond evolved to a single bond from B3-RC to B3-INT. In addition, the hydrogen-bonded network consisting of two auxiliary waters and OH group is revived with the four H-bond distances of 1.928, 1.970, 1.926, and 3.350 Å, respectively. Sequentially, the H_{w2} approaches the O_b leading to a six-membered ring transition state B3-TS2. The imaginary frequency is 842.73 icm^{-1}, which is associated with the coupling of the transfer of H_{b1} atom from O_b to $N_{(2)}$ atom and the transfer of H_{w2} atom from O_w to O_b atom. Finally, there is the product complex B3-PC with the $N_{(2)}$–H_{b1} bond 1.022 Å and a O_b–H_{w2} bond of 0.996 Å. From Table 2, it can be seen that the first process referring to the attacking of the nucleophilic water is the rate-determining step with a barrier height of 34.2 kcal/mol.

3.2.2.4 B-Path 4 As described in Fig. 4, in B4-RC, the H_{w1}, H_{w2}, H_{a1}, and H_{b1} atoms interact, respectively, with the O_a, O_b, $N_{(4)}$, and $O_{(7)}$ atoms to form four hydrogen bonds, with the distances of H_{w1}–O_a, H_{w2}–O_b, H_{a1}–$N_{(4)}$, and H_{b1}–$O_{(7)}$ are 1.997, 1.965, 2.013, and 1.859 Å, respectively. In the ongoing process from B4-RC to B4-TS1, similar to the above mechanism of B-path 3, a six-membered ring transition state is obtained. The imaginary frequency of 1,230.89 icm^{-1} is mainly associated with the transfer of H_{a1} atom from O_a to $N_{(4)}$ atom, the transfer of H_{w1} atom from O_w to O_a atom, and the attacking of O_w at $C_{(1)}$ atom, which intrigues the formation of $C_{(1)}$–O_w bond. After the reaction overcomes the B4-TS1, a tetrahedral intermediate B4-INT emerges along the potential energy profile with the dihedral angle $N_{(6)}$–$N_{(2)}$–$C_{(3)}$–$C_{(1)}$ of −17.9°. The length of $C_{(1)}$–O_w diminishes by 0.132 Å from B4-TS1 to B4-INT, which exhibits that the $C_{(1)}$–O_w bond of B4-INT becomes stronger and the hydroxyl group has been formed. Although H_{b1} interacts with $O_{(7)}$ attached to $C_{(5)}$ atom to offer a hydrogen bond with the distance of 2.268 Å, the H_{b1} atom still can be transferred from O_b to $N_{(6)}$ atom based on the IRC calculation. From B4-RC to B4-INT, the p–π conjugation between $N_{(6)}$ atom and $C_{(1)} = N_{(2)}$ double bond is eliminated, resulting in weakening and elongation of the $C_{(1)}$–$N_{(6)}$ bond. In this process, the energy barrier is 38.7 kcal/mol at the B3LYP level, while it decreases to 34.0 kcal/mol at the MP2 level. In the next step, the transition state B4-TS2, also a six-centered structure, is located in our calculations. The imaginary

frequency is 1,230.89 icm^{-1} and its vibrational mode is mainly associated with the coupling of the transfer of H_{b1} atom from O_b to $N_{(6)}$ atom and the transfer of H_{w2} atom from O_w to O_b atom. As H_{b1} moves from O_b to $N_{(6)}$, the H_{b1} atom is gradually shared by the two heavy atoms, O_b and $N_{(6)}$, through the presence of a proton bridge. In contrast to those of the B4-INT, the transfer of H_{b1} leads to a reduction of 0.046 Å for $C_{(1)}$–O_w bond, as well as a elongation of 0.283 and 0.378 Å for O_w–H_{w2} and O_b–H_{b1} bond length, respectively. After overcame transition state B4-TS2, the product B4-PC is produced. In B4-PC, the $C_{(1)}$–$N_{(6)}$ distance is 3.114 Å, which indicates that this bond has already been broken. The $C_{(1)}$–O_w bond length is 1.241 Å. It is shortened by 0.107 Å compared to that of the B4-TS2, implying that the bond $C_{(1)}$–O_w changes from the single bond to the double bond and the acyl compound has already been formed. In this pathway, the second step corresponding to the proton transfer is the rate-determining step with a barrier height of 40.2 kcal/mol in the gas phase.

3.2.2.5 B-Path 5 As stated in the direct hydrolysis section, the first process of this pathway with regard to the addition of the nucleophilic water to the $C_{(1)}$–$N_{(6)}$ bond is the rate-limiting step, because its relative energy (57.5 kcal/mol) is obviously higher than those in the latter two transition states (being 43.3 and 20.0 kcal/mol for A5-TS2 and A5-TS3, respectively). Accordingly, in this section, for the water-assisted hydrolysis mechanism, we pay more attention to examine the effect of the auxiliary waters in the active site, based on a local microhydration model, on the rate-limiting process. As described in Fig. 5, the reactant complex B5-RC is offered due mainly to the H-bond network, with the distances of H_{w1}–O_a, H_{w2}–O_b, H_{a1}–$O_{(7)}$, and H_{b1}–$N_{(2)}$ are 1.927, 2.089, 1.961, and 2.043 Å, respectively. When the nucleophilic water approaches the $C_{(1)}$ atom, a six-centered transition state B5-TS1 appears along the potential energy profile. The analysis of the vibrational mode indicates that this step is directly associated with the $C_{(1)}$–O_w bond forming, the transfer of H_{w1} from O_w to O_a atom, and the transfer of H_{a1} from O_a to $N_{(6)}$ atom. IRC results further manifest that these three processes occur simultaneously. From B5-RC to B5-TS1, the distances of O_w–H_{w1} and O_a–H_{a1} bond drastically increase to 1.301 and 1.118 Å, respectively, while the $C_{(1)}$–O_w bond reduces remarkably from 3.273 to 1.538 Å. Moreover, from the geometry of B5-TS1, it is clear that the cooperative water plays a decisive role in keeping the nucleophilic water in an efficient position for the reaction and shortens the $C_{(1)}$–O_w distance by 0.335 Å compared to that in direct decomposition mechanism. Sequentially, IRC calculation toward intermediate leads to the emergence of B5-INT1. B5-INT1 is a tetrahedral geometry, and the $C_{(5)}$–$N_{(6)}$ length of 1.768 Å reveals that this bond has already been broken. In this process, the energy barrier diminishes from 57.5 to 46.0 kcal/mol due to the introduction of the auxiliary waters.

According to the energy data in Table 1 and Table 2, as expected, the energy barriers of five water-assisted pathways decrease dramatically about 15–20 kcal/mol as compared to those of the direct pathways because of the contribution of the auxiliary water molecules. Our calculations exhibit that the formation of the favored six-membered ring structure in the transition state leads to the reduction of the ring constraint for the proton transfer, and most of the energy saving has been achieved for its small deformation. In addition, the presence of the cooperative water molecule near to the nonreactive nitrogen atom but not involved in the proton transfer exerts great contribution to keeping the nucleophilic water molecule in an efficient position for the reaction, and the cooperative effect significantly facilitates the nucleophilic attack of H_2O with the $C_{(1)}$–O_w distance being shorter by 0.200–0.300 Å compared with that in the direct hydrolysis reaction.

3.3 Solvent effects of bulk water on the decomposition of 5-azadC

3.3.1 CPCM

In view of the fact that the decomposition of 5-azadC actually takes place in the human body solution, it is of great significance to study the influence of bulk solvent water on the reaction. To estimate this solvent effect in water, the single-point energies were calculated at the MP2/6-311++G(d,p) level by the CPCM model on the basis of the optimized geometries in the gas phase. The relative Gibbs free energies [ΔG(sol)] of five direct (A-paths 1–5) and five water-assisted (B-paths 1–5) pathways are presented in Tables 1 and 2, respectively. From Tables 1 and 2, it can be seen that, both in the direct and in the water-assisted reaction, the rate-controlling step is the first one for those five pathways. Solvent water facilitates the decomposition reaction of 5-azadC, with the transition states in each step of all pathways being stabilized by solvation. For the direct decomposition reaction, the free energy barriers in the rate-controlling step of A-path 1 (48.8 kcal/mol) and A-path 2 (48.8 kcal/mol) are lower than those of other three pathways (being 52.2, 51.5, and 59.0 kcal/mol for A-path 3, A-path 4, and A-path 5, respectively), suggesting that the direct reaction of 5-azadC in water may be favorable for A-paths 1 and 2 than A-paths 3–5.

For the water-assisted decomposition reaction, in step 1 of B-path 1, the free energy barrier is 32.6 kcal/mol in the gas phase, while it decreases to 30.9 kcal/mol in water by solvation. In the first step of B-path 2, the free energy

barriers are 34.9 kcal/mol in the gas phase and 34.6 kcal/mol in solvent water. For B-path 3, the solvent water stabilizes the transition state B3-TS1, leading to a reduction in free energy barrier by 6.8 kcal/mol as compared to that in the gas phase. For B-path 4, the free energy barrier of the first step in water is 2.2 kcal/mol lower than that in the gas phase, indicating that the transition state B4-TS1 is destabilized in solvent water by solvation. In B-path 5, for the first step, the free energy barrier is 48.6 kcal/mol in the gas phase, while it diminishes to 41.9 kcal/mol in water. Due to the contribution of the auxiliary water molecules, among five examined water-assisted pathways, B-path 3 becomes the most favorable one and $\Delta G^{\neq}$(sol) in the rate-limiting step of five pathways increases in the order: B-path 3 (28.2 kcal/mol) < B-path 1 (30.9 kcal/mol) < B-path 2 (34.6 kcal/mol) < B-path 4 (36.7 kcal/mol) < B-path 5 (41.9 kcal/mol).

3.3.2 Monte Carlo simulations

In this work, Monte Carlo method with FEP technique was performed to simulate the above five water-assisted decomposition reactions in water. The changes in free energies of solvation for the activation and reaction procedures are given in Table 2. Figure 6 depicts the relative potential energy profiles $E_{\mathrm{MEP}}(s)$ of the reaction paths along the minimum energy path (MEP) in the gas phase and in water. From Table 2 and Fig. 6, one can see obviously that, among the five examined pathways, the solvent effect remarkably decreases the energy barriers of B-path 3. The energy data in Table 2 show that the free energies of activation of the rate-limiting steps of five pathways were calculated by combining B3LYP/6-31+G(d,p) calculation with Monte Carlo simulation and increase in the following order: B-path 3 (19.6 kcal/mol) < B-path 1 (27.1 kcal/mol) < B-path 2 (30.7 kcal/mol) < B-path 4 (41.5 kcal/mol) < B-path 5 (44.8 kcal/mol). It is clear that B-path 3 has the highest possibility to occur in the water-assisted decomposition reaction of 5-azadC when the solvent effects of bulk water are taken into account, which is in agreement with those results obtained by the SCRF (CPCM model) method.

In addition, for B-path 3 and B-path 1, the water environment has similar effect on the rate-determining steps but decreases the former more the activation free energy by 13.8 kcal/mol than that of the latter. This indicates that B-path 3 has more advantage than B-path 1 in the aqueous solution as compared with the gas phase. To account for this, the solute–water pair energy distributions (PED) for the rate-limiting steps of B-path 3 and B-path 1 were plotted in Fig. 7. The plots give the number of solvent molecules on the *y*-axis that interact with the solute with the interaction energy shown on the *x*-axis. The bands at low energy result from the hydrogen-bonded solvent molecules and the spike centered at 0.0 kcal/mol comes from the weak interactions between the solute and many distant solvent molecules in outer shells. As presented in Fig. 7, for B-path 1, there is a bound group of solvent molecules, which forms a band from ca. −15.0 to −7.0 kcal/mol. Integration of the distribution curve for B1-RC, B1-TS1, and B1-INT until this limit results in 1.76, 2.28, and 2.03 water molecules that interact with solute. The numbers of water interacting with solute increase by 0.52, leading to the slight decrease in the energy barrier in the first step of B-path 1 in bulk water. For B-path 3, hydrogen bonding in water is reflected in the left most region with energies more attractive than ca. −3.0 kcal/mol. The hydrogen-bonded energy band for B3-RC in water covers the range from −14.0 to −3.0 kcal/mol. Integration of the curves up to the end of the plateaus at −3.0 kcal/mol forms 7.17, 8.61, and

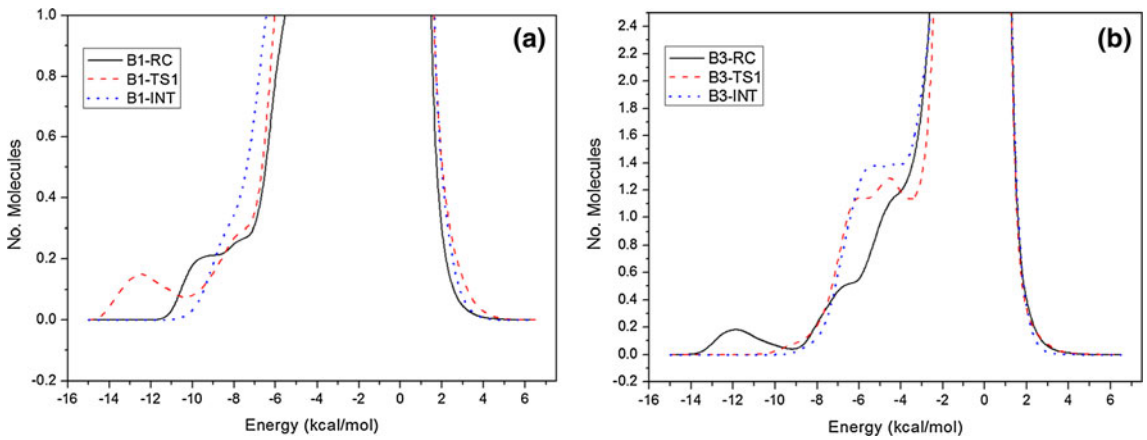

Fig. 7 Pair energy distributions of the solute–water interaction for the rate-limiting steps of the water-assisted B-path 1 (a) and B-path 3 (b) of 5-azadC in water

8.30 water molecules for B3-RC, B3-TS1, and B3-INT, respectively. The numbers of water strongly interacting with solute increase by 1.44 on going from B3-RC to B3-TS1, whereas the change is only 0.52 for B-path 1. The differences imply that the solvation of the transition state B3-TS1 is better than that of B1-TS1, lowering the more energy barriers in the rate-limiting step of B-path 3 in bulk water.

According to our calculated free energy barrier in solution, the classical rate constant can be calculated by the Eyring equation given by the activated complex theory [38]

$$k = \frac{k_B T}{h} \exp\left(\frac{-\Delta G^{\neq}}{RT}\right) \quad (4)$$

The calculated rate constant of the most favorable water-assisted B-path 3 is 0.79×10^{-3} min^{-1} at the SCRF (CPCM model) method and 1.68×10^{-3} min^{-1} at the MC-FEP method. The comparison of our results with experimental data ($(5.89 \pm 0.54) \times 10^{-3}$ min^{-1} by UV and $(1.46 \pm 0.08) \times 10^{-3}$ min^{-1} by NMR) [19] shows that our estimation for the rate constant at the SCRF(CPCM model) method (0.79×10^{-3} min^{-1}) is slightly lower than the experimentally determined value, while the rate constant at the MC-FEP method (1.68×10^{-3} min^{-1}) is within the range of the experimental value.

4 Conclusion

In this study, the decomposition mechanism of 5-azadC in water was investigated at the B3LYP/6-31+G(d,p) and MP2/6-311++G(d,p)//B3LYP/6-31+G(d,p) levels of theory in the gas phase. Five possible pathways (paths 1–5) were taken into account. In each pathway, two types of reaction processes were explored. One is a direct decomposition with one water molecule (A-paths 1–5) and the other is a water-assisted decomposition based on a microhydration model with three water molecules (B-paths 1–5). Our computed results clearly manifest that zero-point vibrational energy barriers ($\Delta E^{\neq}$) and Gibbs free energies ($\Delta G^{\neq}$) in each step of the water-assisted pathways decrease dramatically by about 15–20 kcal/mol as compared with those of the direct pathways in the gas phase. In addition, the solvent effect of bulk water was evaluated by the SCRF (CPCM model) and MC-FEP methods. The results indicated that, at the MC-FEP method, the presence of water as the solvent results in a net stabilization of B-path 3, which is consistent with the SCRF (CPCM model) result but energetically preferred to the SCRF (CPCM model) method. Out of five examined water-assisted pathways, B-path 3 has the highest possibility to occur, which with the attack of nucleophilic water at the $C_{(1)}$ atom corresponds to the proton movement toward the $N_{(4)}$ atom to form a tetrahedral intermediate B3-INT. Subsequently, a ring-opening product B3-PC is generated through the transfer of hydroxyl H atom to the $N_{(2)}$ atom. The calculated rate constant (1.68×10^{-3} min^{-1}) of B-path 3 at the MC-FEP method is acceptable within the experimental range. Such calculations give out a greater fundamental understanding for this important biological reaction. Our results may facilitate ongoing clinical development aimed at understanding the mechanism of toxicity and potential mutagenicity of 5-azadC and related analogues.

Actually, the decomposition of 5-azadC as a drug takes place in the human body solution. Experimentally, this decomposition reaction was usually investigated and characterized in water and in plasma. To mimic the biological environment, only water has been chosen as solvent in our calculations. The effects of other solvent like methanol on the decomposition of 5-azadC were not the focus in this study. So, here we did not consider the solvent effect in methanol or a mixture of water and methanol. The effects of other solvents on the decomposition of 5-azadC will be studied in our future work.

Acknowledgments This project has been supported by the National Natural Science Foundation of China (Grant Nos. 21173151 and 20835003).

References

1. Sorm F, Piskala A, Cihak A, Vesely J (1964) Experientia 20:202–203
2. Issa J-P, Garcia-Manero G, Giles FJ, Mannari R, Thomas D, Faderl S, Bayar E, Lyons J, Rosenfeld CS, Cortes J, Kantarjian HM (2004) Blood 103:1635–1640
3. Balch C, Yan P, Craft T, Young S, Skalnik DG, Huang TH, Nephew KP (2005) Mol Cancer Ther 4:1505–1514
4. Ruter B, Wijermans PW, Lubbert M (2006) Cancer 106:1744–1750
5. Kantarjian H (2006) Issa J-P J, Rosenfeld CS, Bennett JM, Albitar M, DiPersio J, Klimek V, Slack J, de Castro C, Ravandi F, Helmer R, Shen L, Nimer SD Leavitt R, Raza A, Saba H. Cancer 106:1794–1803
6. Momparler RL, Bouffard DY, Momparler LF (1997) Anticancer Drugs 8:358–368
7. Thibault A, Figg WD, Bergan RC, Lush RM, Myers CE, Tompkins A, Reed E, Samid D (1998) Tumori 84:87–89
8. Jubb AM, Bell SM, Quirke PJ (2001) Pathol 195:111–134
9. Jüttermann R, Li E, Jaenisch R (1994) Proc Natl Acad Sci USA 91:11797–11801
10. Christman JK (2002) Oncogene 21:5483–5495
11. Cho HJ, Kim SY, Kim KH, Kang WK, Kim JI, Oh ST, Kim JS, An CH (2009) World J Surg Onc 7:49–55
12. Schermelleh L, Spada F, Easwaran HP, Zolghadr K, Margot JB, Cardoso MC, Leonhardt H (2005) Nat Methods 2:751–756

13. Ghoshal K, Datta J, Majumder S, Bai S, Kutay H, Motiwala T, Jacob ST (2005) Mol Cell Biol 25:4727–4741
14. Patel K, Dickson J, Din S, Macleod K, Jodrell D, Ramsahoye B (2010) Nucleic Acids Res 38:4313–4324
15. Lin K-T, Momparler RL, Rivard GE (1981) J Pharm Sci 70:1228–1232
16. Vesely J, Piskala A (1984) Cancer Res 44:5165–5168
17. Liu ZF, Marcucci G, Byrd JC, Grever M, Xiao J, Chan KK (2006) Rapid Commun Mass Spectrom 20:1117–1126
18. Pithová P, Pískala A, Pitha J, Šorm F (1965) Collect Czech Chem Commun 30:2801–2811
19. Rogstad DK, Herring JL, Theruvathu JA, Burdzy A, Perry CC, Neidigh JW, Sowers LC (2009) Chem Res Toxicol 22:1194–1204
20. Gao JY, Zeng Y, Zhang CH, Xue Y (2009) J Phys Chem A 113:325–331
21. Xue Y, Kim CK (2003) J Phys Chem A 107:7945–7951
22. Xue Y, Kim CK, Guo Y, Xie DQ, Yan GS (2005) J Comput Chem 26:994–1005
23. Xue Y, Zhang H, Xie DQ, Yan GS (2005) Chem J Chin U 26:907
24. Wu Y, Xue Y, Xie DQ, Kim CK, Yan GS (2007) J Phys Chem B 111:2357–2364
25. Xia XF, Zhang CH, Xue Y, Kim CK, Yan GS (2008) J Chem Theory Comput 4:1643–1653
26. Chen ZQ, Xue Y (2010) J Phys Chem B 114:12641–12654
27. Fukui K (1970) J Phys Chem 74:4161–4163
28. Breneman CM, Wiberg KB (1990) J Comput Chem 11:361–373
29. Frisch MJ, Trucks GW, Schlegel HB, Scuseria GE, Robb MA, Cheeseman JR, Montgomery Jr JA, Vreven T, Kudin KN, Burant JC, Millam JM, Iyengar SS, Tomasi J, Barone V, Mennucci B, Cossi M, Scalmani G, Rega N, Petersson GA, Nakatsuji H, Hada M, Ehara M, Toyota K, Fukuda R, Hasegawa J, Ishida M, Nakajima T, Honda Y, Kitao O, Nakai H, Klene M, Li X, Knox JE, Hratchian HP, Cross JB, Bakken V, Adamo C, Jaramillo J, Gomperts R, Stratmann RE, Yazyev O, Austin AJ, Cammi R, Pomelli C, Ochterski JW, Ayala PY, Morokuma K, Voth GA, Salvador P, Dannenberg JJ, Zakrzewski VG, Dapprich S, Daniels AD, Strain MC, Farkas O, Malick DK, Rabuck AD, Raghavachari K, Foresman JB, Ortiz JV, Cui Q, Baboul AG, Clifford S, Cioslowski J, Stefanov BB, Liu G, Liashenko A, Piskorz P, Komaromi I, Martin RL, Fox DJ, Keith T, Al-Laham MA, Peng CY, Nanayakkara A, Challacombe M, Gill PMW, Johnson B, Chen W, Wong MW, Gonzalez C, Pople JA (2005) Gaussian 03. Version D01. Gaussian, Inc., Wallingford CT
30. Barone V, Cossi M (1998) J Phys Chem A 102:1995–2001
31. Jorgensen WL, Ravimohan C (1985) J Chem Phys 83:3050–3054
32. Jorgensen WL, Chandrasekhar J, Madura JD, Impey RW, Kelin ML (1983) J Chem Phys 79:926–935
33. Duffy EM, Severance DL, Jorgensen WL (1992) J Am Chem Soc 114:7535–7542
34. Kaminski GA, Jorgensen WL (1998) J Phys Chem B 102:1787–1796
35. Jorgensen WL (1986) J Phys Chem 90:1276–1284
36. Zwanzig RW (1954) J Chem Phys 22:1420–1426
37. Jorgensen WL, Tirado-Rives J (2005) J Comput Chem 26:1689–1700
38. Eyring H (1935) Chem Rev 17:65–73